EXPERIMENTAL AND NUMERICAL STUDY OF THE DYNAMIC BEHAVIOUR OF MASONRY CIRCULAR ARCHES WITH NON-NEGLIGIBLE TENSILE CAPACITY

ALEJANDRA ALBUERNE[1], ATHANASIOS PAPPAS[2], MARTING WILLIAMS[3] AND DINA D'AYALA[2]

[1] Institute for Sustainable Heritage, University College London, London (UK)
[2] Department of Civil, Environmental and Geomatic Engineering, University College London (UK)
[3] Department of Engineering Science, University of Oxford (UK)

Abstract

Continuous arches and vaults made of cohesive materials with low but non-zero tensile strength, such as Roman concrete, are a common feature in historic and monumental structures, many of them sited in earthquake-prone regions. The effect of tension capacity on the dynamic behaviour of masonry vaulted structures has scarcely been studied. We describe a series of shaking table tests on model-scale, continuous circular arches of 1m span, with the aims of assessing the effect of tensile capacity on mechanism formation, evaluating the structures' lateral acceleration capacity and comparing their performance to that of voussoir arches. While tested arches fail by forming a four-link mechanism like the no-tension voussoir arch, significant differences in behaviour between continuous and voussoir arches are observed, including: differences in hinge positions; higher accelerations required to initiate rocking; cracking of material required to form hinges; inability of hinges, once formed, to close and move to a different location (travelling hinges). Conventional limit analysis, whose basis includes an assumption of zero tensile strength, is a suitable analytical tool for voussoir arches, but is shown to be inaccurate when applied to arches having a modest tensile capacity. The experimental observations are modelled using non-linear finite elements Abaqus/Explicit dynamic analysis algorithm, from commercial software Abaqus 2017. By applying the Concrete Damage Plasticity numerical material law, good agreement is obtained between the tests and the numerical predictions, supporting the formation of collapse mechanisms that significantly differ from the mechanisms observed for no-tension arches. Finally, the numerical model is upscaled to study full-size arches with a span of 4m, obtaining results that align with the experimental observations and do not agree with observations and models for the no-tension voussoir arch, evidencing the need to account for tensile capacity of vaulted structures when assessing their dynamic capacity.

1. Introduction

Modern analysis of masonry structures under the framework of plastic theory was established in the second half of the 20th century (Kooharian 1952, Heyman 1966). It treats masonry as rigid and embraces the three classic axioms stated in the 18th century by Couplet (1729): 1) infinite compressive strength; 2) zero tensile strength; 3) there is no sliding. Under these premises, the only possible failure for a masonry structure is through the formation of a kinematically admissible mechanism by developing rotational hinges. Such mechanism depends purely on geometry and loading conditions, including self-weight.

The axioms that support this theory are simplifications of the material properties that respond to observations of masonry failure over time. They are, however, open to question. As early as 1806, Monasterio explored the possibility of sliding failure in mechanism formation (Albuerne & Huerta 2010). More recently, Livesley (1978) formulated limit analysis for 2D block structures accounting for frictional forces on the interfaces. Livesley (1992) extended this analysis to 3D arches introducing

Coulomb friction at the block interfaces. Casapulla & D'Ayala (2001) incorporated non-symmetric loading in order to establish when sliding failure becomes a limiting factor.

The axiom of 'zero tensile strength', is commonly redefined as 'zero tensile strength at the joints' (Boothby 2001), recognising that masonry blocks do resist tensile stresses and hinges tend to open at the joints, where the mortar is typically weaker, may have experienced decay or may not be present. Under this assumption, hinges are free to form at any joint in the structure. There are, however, numerous masonry constructions that present a level of tensile strength at joints exerting a resistance against separation of masonry blocks. An important category of vaulted structures exhibiting some tensile strength is ancient Roman construction made of Roman concrete, as exemplified by the remains of the Basilica of Maxentius in Rome (Giavarini 2005, Albuerne & Williams 2017).

The failure of vaulted structures with a moderate capacity to withstand tensile forces has received limited attention in the literature. While zero tensile strength may be a safe assumption for structures under static loads (Heyman 1966), its safety for structures subject to dynamic loading has not been demonstrated.

Smars (2000, 2008) explores the applicability of limit analysis to vaulted structures that feature both some tensile strength and finite friction and proposes the existence for certain structures of a "potentially stable" domain in addition to the classic stable and unstable domains.

More recently, Ramaglia et al. (2016) explored the problem applied to barrel vaults subject to dynamic lateral loading and proposed accounting for tensile strength in limit analysis by applying an expansion of the boundaries of permissible positons of the line of thrust. This simplified model does not account for the quasi-brittle nature of typical masonry materials. These materials experience an immediate drop in strength post crack initiation that leads to a redistribution of stresses after every crack forms. As a result, in the general cases the maximum moment capacity is not experienced simultaneously at all hinges.

This paper explores the effect that moderate tensile strength has on the failure of vaulted masonry structures subject to dynamic loading. The paper describes novel shaking table tests on cohesive, continuous arches made of quasi-brittle material and subject to cyclic base motion, comparing their performance to that of zero-tension voussoir arches. It further presents the results of a fully dynamic computational analysis using Non-Linear Finite Elements (NLFE) carried out to understand the experimental findings regarding the formation of the first hinge through the opening of a crack.

2. Dynamic behaviour of the voussoir circular arch

The study of the no-tension voussoir or dry-joint arch is an insightful step towards understanding the behaviour of vaulted masonry structures. It has been explored in the literature as a fundamental element of masonry vaulted systems, with a particular focus on the constant-thickness circular arch, as related in this section. The circular arch has a simple geometry that can be easily constructed using similar voussoirs, be these cut stones or bricks. This arch has been used repeatedly throughout the history of construction in buildings, gates or bridges. It often features fill on the extrados, in particular in bridges, which can have a significant impact on its structural behaviour, as explored by Pulatsu et al. (2019). Addressing the arch by itself, without including the effect of fill and isolating it from the performance of abutment systems, is a significant step in exploring the mechanical performance of masonry structures, as it does not introduce additional complexities (Heyman 1969) and thus the findings are easier to interpret. The study of the circular arch by itself is primarily a theoretical question that contributes towards understanding the capacity of masonry vaulted structures.

The stability of simple arches has been examined for centuries (see Huerta 2004 for a detailed account). From the formulation of plastic theory for masonry by Heyman (1966), limit analysis has been applied

to examine simple circular arches in 2D under the three fundamental axioms (e.g. Heyman 1969, Oschendorf 2002, Makris & Alexakis 2013), as well as considering possible sliding failure (e.g. Livesley 1998). The problem has been studied in 3D by authors including Smars (2000), Casapulla & D'Ayala (2001), exploring the effect of finite Coulomb friction and eccentric loading, concluding that friction is the limiting parameter in a range of not uncommon occasions.

The behaviour of the voussoir arch under seismic lateral loads has been explored more rarely. Static-equivalent approaches aimed at identifying the minimum horizontal load required to initiate a mechanism in a circular arch when acting in combination with gravity loads have been explored by authors including Otto (1983), Oppenheim (1992), Clemente (1998), Ochsendorf (2002) or Alexakis and Makris (2014). Most studies of this problem employ energy formulations to determine the point of mechanism formation.

Shaking table tests to explore the dynamic behaviour of voussoir arches have been reported by de Lorenzis et al (2007), DeJong & Ochsendorf (2010), Albuerne et al (2013) and Gaetani et al. (2017). A non-symmetric four-hinge mechanism, hereon referred to as 4-link mechanism, has been observed to form (see Fig. 1), with hinge *D* systematically opening on the extrados at one of the supports and hinge B opening near the crown. The phenomenon of *travelling hinges* is normally observed, with hinges shifting from one joint to the next as the motion progresses.

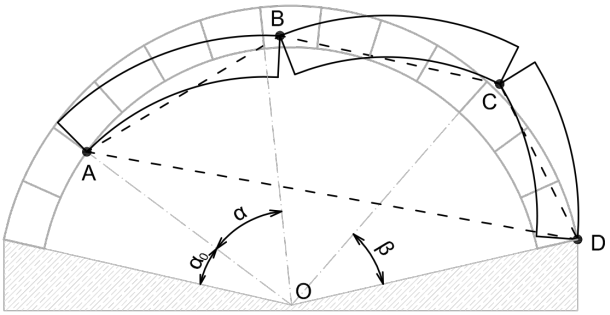

Fig. 1. Typical four-link mechanism failure for zero-tension voussoir arch.

The dynamic behavior of arches has been studied analytically. Oppenheim (1992) developed an analytical model for the behaviour of the arch 4-link mechanism during the first half-cycle of a cyclic base motion, before the first impact of the rocking motion occurs. The model was extended by de Lorenzis et al (2007) to include behaviour after impact, presuming that the mirror mechanism will open as rocking reverses.

Different computational approaches have been applied to modelling the dynamic response of voussoir arches. Discrete Element Modelling (DEM) has been frequently adopted as the most effective computational framework for modelling discontinuities and capturing the mechanics of loose block structures (Lemos 2007). DEM have been applied to study the dynamics of no-tension voussoir arches subject to base motion (e.g. Lemos 2001, Alexakis & Makris 2016), obtaining good agreement between modelling and experimental results (e.g. DeJong et al. 2008, Albuerne et al 2013). The development of (NLFEM) has enabled the application of Finite Element Modelling (FEM) to the problem of collapse of dry-joint masonry structure. See section 4.1 for a brief review of the literature.

In spite of the deep interest of the dynamic performance of the dry-joint voussoir arch, in many vaulted structures the material exhibits some bond between the blocks. As a result, hinges are not 'free' to open at any joint in the structure and must be the result of fracture of the material. In the following sections, the behaviour of vaults with (low) tensile strength is explored.

3. Experimental tests on circular arches with non-negligible tensile strength

Semi-circular continuous arches were subject to cyclic base motion on a shaking table, testing samples to increasing load until cracking and subsequent collapse occurred. This section summarises the construction and testing procedure.

3.1 Geometry of arch specimens

Specimens were semi-circular arches (angle of embrace of 180°), with parallel intrados and extrados, and internal span of 900 mm, Fig. 2. Three different thicknesses were tested: t = 62 mm (giving t/r_m = 0.13), t = 67 mm (t/r_m = 0.14) and t = 72 mm (t/r_m = 0.15).

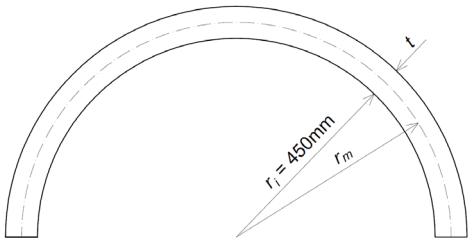

Fig. 2. Semi-circular arch geometry

3.2 Material of arch specimens

Arches were made of a quasi-brittle mortar having natural hydraulic lime (NHL 5.0) as binder and washed sharp sand (average particle size of 1.2mm) as aggregate. This material aimed to replicate the behaviour of moderately cohesive masonry in the fashion of Roman concrete. The tensile strength was kept as low as practically possible for handleability considerations. The average ratio of lime–sand–water by volume was 1–3.2–0.88, with small variations in water content to achieve desirable workability of the mix.

The material properties were characterised through a testing campaign of three-point bending tests on pre-notched samples 300 mm long and 50 x 50 mm cross-section. A series of 35 control samples with lime-sand volume ratio of 1-3.2 were tested (see Fig. 12 for summary of results). As a quasi-brittle material, the mortar exhibits a progressive drop in strength with increased deformation beyond the point of maximum load (Karihaloo & Huang 1991), as shown in the typical test result in Fig. 3. The exact form is dependent on mix details and on the internal micro-structure, that is, the number, size and distribution of internal pores and cracks (Shah & Ouyang 1994). An inherent variability in the values of peak load and curve shape between different samples of the same material has been observed, resulting in a variability of tensile strength f_t and fracture energy G_f, consistent with other tests on modern concrete, also a quasi-brittle material, and reproductions of ancient Roman mortar (Samuelli Ferretti 2000, Brune 2010). The mean material properties of the mortar mix were: density 1870 kg/m^3, compressive strength 1.65 MPa, tensile strength 0.426 MPa (SD: 0.108 or 25.3%) and fracture energy 7.85 Nm/m^2 (SD: 2.67 or 34.0%). The tensile strength is obtained as the peak tensile strength experienced by the test sample, calculated using the maximum bending moment recorded in the bending moment vs curvature plot for each three-point bending test. The fracture energy is obtained by computing the area under the bending moment vs curvature curve, introducing the corrections given by Planas & Elices (1985) and Rodriguez del Viso (2008). The standard deviation values reflect the inherent variability of the material properties.

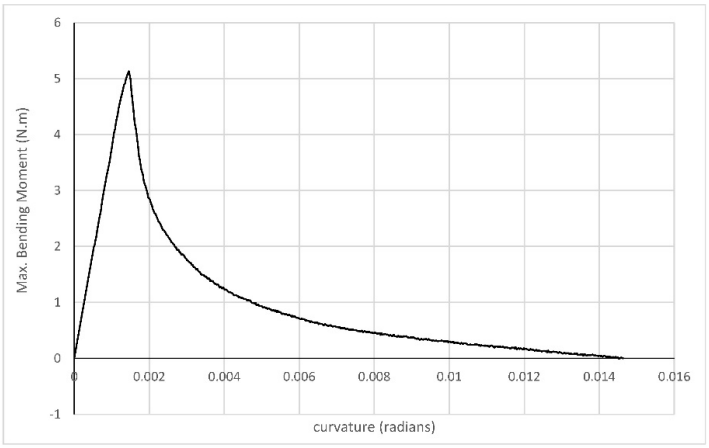

Fig. 3. Corrected moment-rotation curve for a three-point-bending test of lime mortar used in test specimen construction

Based on scaling theory, the scaling relationship can be obtained by considering a vertical cantilever (density ρ, length L, cross-sectional depth d) subject to inertial lateral acceleration, a (Albuerne 2016). The ratio of fracture stress f_f to bending stress f_b is given by:

$$\frac{f_t}{f_b} = \frac{f_f \cdot d}{3\,L^2\,\rho\,a} \qquad \text{[Eq. 1]}$$

This ratio should be preserved in the test specimen. Using '*' to represent the quantities in the test specimen compared to the un-starred real prototype values:

$$\frac{f_f^*\,d^*}{3\,L^{*2}\,\rho^*\,a^*} = \frac{f_f\,d}{3\,L^2\,\rho\,a} \qquad \text{[Eq. 2]}$$

Given that linear dimensions will scale the same and that accelerations scale at unity (to preserve similitude of stresses due to gravity and lateral acceleration), the resulting scaling relationship for these model arches is given by:

$$\frac{f_t^*}{f_t} = \frac{\rho^*}{\rho} \cdot \frac{L^*}{L} \qquad \text{[Eq. 3]}$$

Taking Roman concrete as a reference material, we obtain that the density ratio is approximately equal to unity while the tensile strength of the real material as tested by Giavarini et al. (2006) is 2 to 3 times higher than the characteristic value for the lime mortar (Table 1). This results in the test specimen being representative of real Roman concrete arches with 2 times larger span, i.e. a span length of approximately 2 m.

Table 1. Material properties of mortar used in experiments compared with available strength tests performed on original Roman concrete samples

Sample	Compressive Strength (MPa)	Tensile Strength (MPa)	Vol. Mass Density (kN/m^3)
Lime mortar Lime:Sand:Water(V) 1:3.2:0.88	1.65	0.426 (S.D. 0.108)	18.7
Hadrian's Villa[†] Vaults of *Sala a tre essedre*	4.5	0.77	17.7

Hadrian's Villa[†] Vaults of *Sala a tre essedre*	5.87	0.88	17.7

[†]Test results from Giavarini et al. (2006)

3.3 Test procedure

Tests were performed on a uniaxial shaking table in the Oxford Structural Dynamics Laboratory (Univeristy of Oxford), comprising a 1 m square platform running on horizontal linear bearings. It is driven by a single 10 kN Instron servo-hydraulic actuator that can apply uni-directional displacement amplitudes up to ±75 mm. Arches were simply supported on the table, with sliding prevented by padded brackets placed on both sides of the supports (Fig. 4). These support conditions could be representative of arches and vaults supported on metal brackets or beams, such as is sometimes encountered in 19th and early 20th timbrel vaults. In the case of masonry vaults with continuity down the supports, such as Roman concrete structures, these support conditions represent a singular theoretical case in which cracks exist at the base of the arch. While real structures are commonly cracked, the typical crack pattern for a circular arch comprises three cracks, with a crack at midspan and a crack at each support. The present setup without the midspan crack is nonetheless an interesting case to analyse as the degree of static indeterminacy is reduced to 1, which simplifies the study.

Fig. 4. Support conditions for arch samples on shaking table with rubber padded metal brackets on both intrados and extrados to prevent sliding, while a degree of rotation can be expected.

While elastic response spectra are not appropriate for identifying the seismic response of highly inelastic structures (Douglas et al 2015) pulse-type excitations representing the principal impulse of an earthquake wave have been found to be appropriate simplifications of near-source ground motions for appraisal of rocking structures (DeJong & Ochsendorf 2010, Makris & Roussos 2000, Campillo et al. 1989). Given their continuous derivatives, sine pulses were chosen, in agreement with Zhang & Makris (2001) and Gaetani et al (2017). To prevent large acceleration spikes at the start and end of the test, ramped attack and decay cycles were added as shown in Fig. 5 (Williams et al. 2012).

Because tests involved large motions, fracture and collapse, particle image velocimetry (PIV) was used to track the motion of the specimens. GeoPIV software by White et al (2003), which is based on high-density-image and single-exposure multi-frame PIV and is designed to be applied to conventional (non-rectified) digital images. A speckle pattern was applied to the front face of each arch to facilitate accurate tracking and a reference static grid was introduced to provide scale (see Fig. 6). A black-and-white high-speed camera was used, recording 250 fps (time step 4 ms) at a resolution of 1024 x 512 pixels. Further details of the PIV implementation can be found in Albuerne & Williams (2015).

Differences were observed between the ideal input motion (Fig. 5) and the motion observed by the tested arches (Fig. 6). These are caused by the shaking table controller, which rectifies the actuator motion to correct the displacement. The parameters of the controller were adjusted to prioritise a smooth acceleration wave.

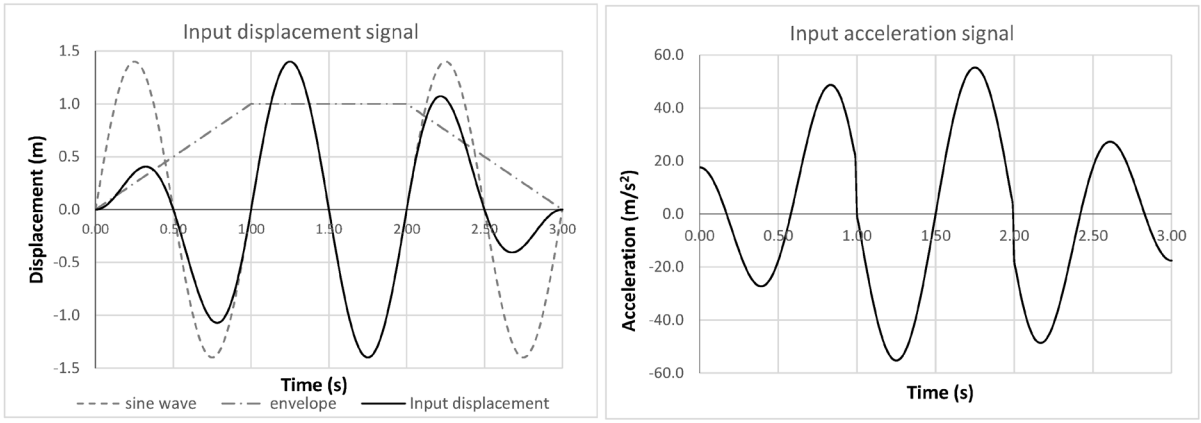

Fig. 5. Input displacement signal (left); and corresponding input acceleration (right). Scaled to the appropriate amplitude and frequency at time of testing. Note discontinuities in gradient of acceleration signal, resulting from the second derivative of the envelope applied to displacement signal.

3.4 Experimental results

Arches were tested under pulses of increasing amplitude and/or frequency until accelerations that generated crack formation and subsequent collapse were reached. In this section the main observed failure mechanism is described and the acceleration levels required to cause failure are presented. The differences in behaviour between continuous arches and discrete voussoir arches are highlighted.

The mode of failure of tested arches is by forming a four-link mechanism, as illustrated in Fig. 6. This shows snapshots of arch deformation showing how deformations vary with time, the corresponding mechanism diagrams and the displacement and acceleration time signal. The time signal plots present the displacement and acceleration recorded for the top centre section of the arch (in bold) and the command signal sent to the table (lighter dashed line). As expected, the signals diverge significantly as the arch collapses, after around 0.5 s. Imperfect actuator control results in the introduction of a higher frequency component in the motion, most clearly visible in the acceleration plot. The numbering i–iv below refers to the photos in Fig. 6:

i–ii. As the acceleration reaches a peak, hinges open in positions *B* (crack opening on the intrados) and *C* (crack opening on the extrados). Together with the hinges at the two supports, a four-hinge mechanism is formed. Close examination of high-speed camera images reveals that the crack that forms hinge *B* becomes visible before that for hinge *C*.

iii–iv. The arch may then either directly collapse, toppling in the direction of the acceleration that generated the mechanism, or (more often) rock to collapse in the following half cycle, its motion having reversed. In a small number of tests, the arch rocked repeatedly, returning to its equilibrium position at the end of the test.

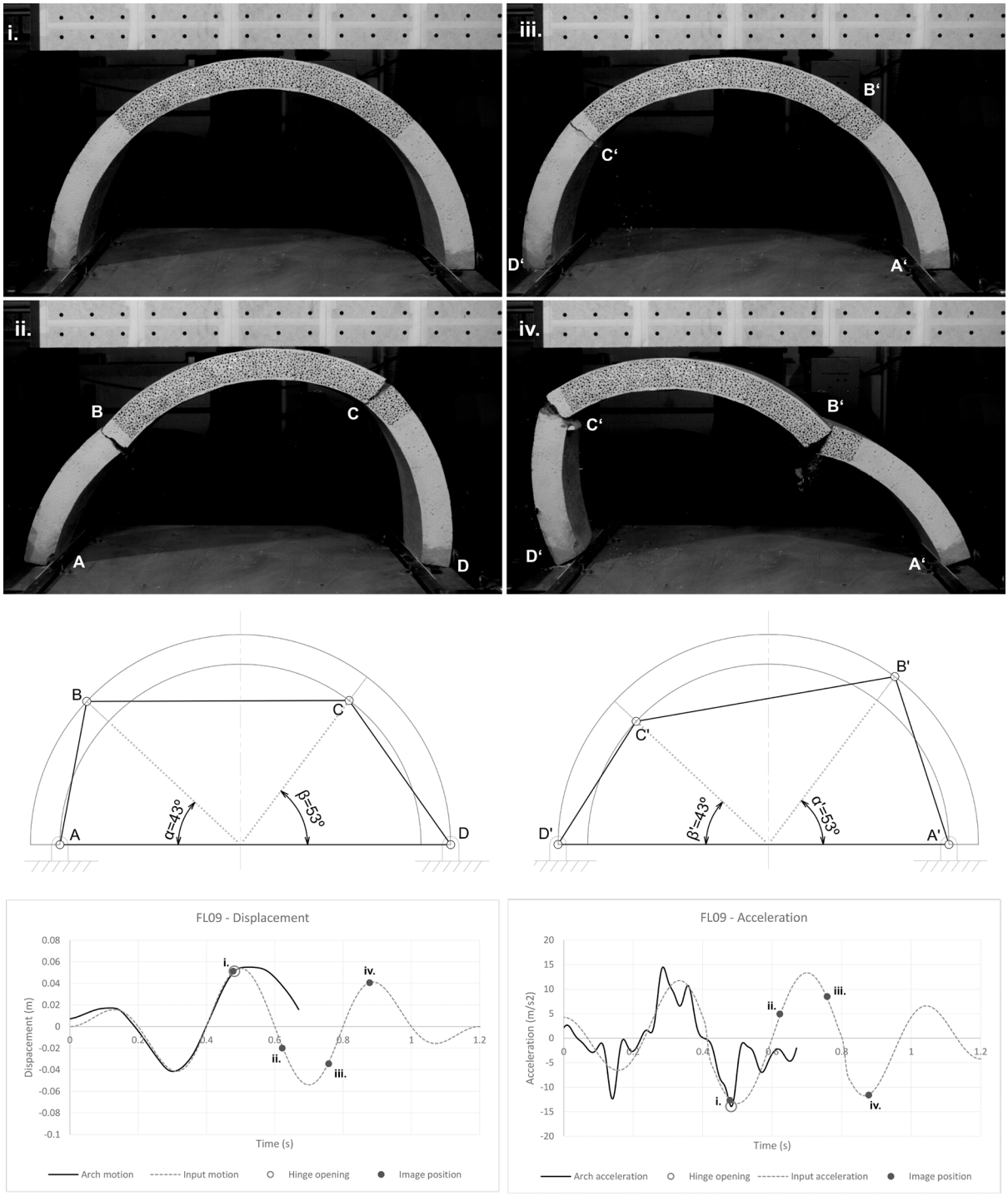

Fig. 6. Hinge formation and collapse of tested arch by forming a 4-link mechanism (test specimen FL9): i – iv steps in the collapse; diagrams of initial 4-link mechanism and subsequent reversed mechanism; Displacement and acceleration at centre of arch, showing the position of images i – iv and the formation of cracks. Image (i.) is taken an instant before cracks form at positions B and C, seen on image (ii.).

Table 2 summarises the ten tests failing by mobilisation of a four-link mechanism. The horizontal acceleration at onset of the mechanism (i.e. crack formation) and the hinge positions are provided. There is a degree of variability in acceleration at the onset of cracking that is understood to be directly related to the variability of the material discussed in section 3.1. The standard deviation in acceleration at hinge

formation corresponds to 4.1% for t/r_m = 0.13; 8.7% for t/r_m = 0.14; and 17.8% for t/r_m = 0.15, all smaller than the standard deviation for the material properties f_t and G_f.

Hinge positions for the tested arches are illustrated in Fig. 7. Hinges *A* and *D* open at the supports, where there is no resistance to rotation. Hinges *B* and *C* open on either side of the centreline of the arch, at significantly similar distance. This is different from the minimum horizontal acceleration mechanism obtained for the zero-tension voussoir arch, shown in Fig. 8 for the same *t/r = 0.15*, discretized into 15 equal voussoirs. This mechanism is calculated using limit analysis for the voussoir arch subject to gravity and inertial loads caused by the minimum lateral acceleration required to mobilise a mechanism (Ochsendorf 2002), applying the method of graphic statics. Dejong & Ochsendorf (2010) observed the limit analysis mechanism to match that observed in experimental dynamic tests.

The position of hinges *B* and *C* also presents variability between tests. The observed location of each of these hinges lies within a bracket of approximately 20°. This variation is exemplified in the difference between tests FL8 and FL9, identified in colour in Fig. 7. While the acceleration at crack formation for these two tests is very close, the position of the hinges is visibly different. Hinge *C* opens almost at the same place, while hinge *B* is shifted by 8°, resulting in different angle *BOC* (75° for FL8 and 84° for FL9). Another example is found in comparing tests FL3 and FL4, also experiencing cracking at similar levels of lateral acceleration. In this case, the angle *BOC* is similar in both tests (69° for FL3 and 66° for FL4), but is shifted by 10° towards hinge *D*.

These differences in position are linked to the aforementioned variability of the material, together with the dynamic nature of the loading. The random distribution of the microstructure of the material can lead to the existence of points along the arch where crack initiation is more likely. The distribution of internal stresses within the arch is constantly changing throughout the shaking table test, with the position of maximum stresses shifting along the arch.

Table 2. Summary of results for tests showing four-hinge mechanism (see Fig. 1 for definitions of hinges *B* and *C*; see Fig. 7 for Test FL9)

Test	t/r_m	Accn at hinge formation (x *g*)	Hinge position (angle from base)	
			Hinge *B*	Hinge *C*
FL1[†]	0.13	1.12	52°	55°
FL2	0.13	1.00	57°	49°
FL3	0.13	1.07	52°	59°
FL4[*]	0.13	1.05	62°	52°
FL5	0.14	1.44	67°	61°
FL7	0.14	1.21	61°	41°
FL8[†]	0.15	1.42	51°	54°
FL9	0.15	1.42	43°	53°
FL10	0.15	1.49	53°	44°
FL11	0.15	0.91	51°	41°

[†] Direct collapse without rocking

[*] Return to equilibrium after rocking

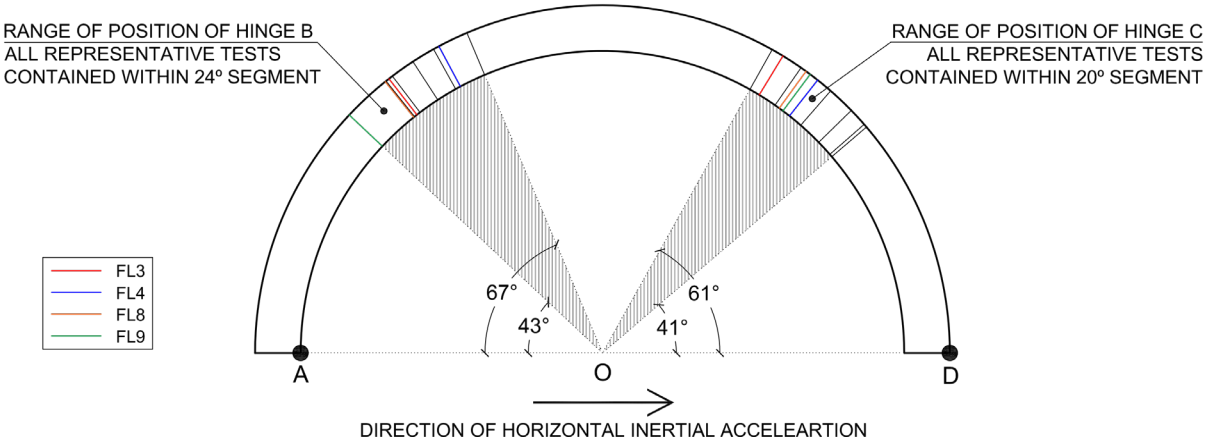

Fig. 7 Summary of hinge positions for tests forming a 4-link mechanism.

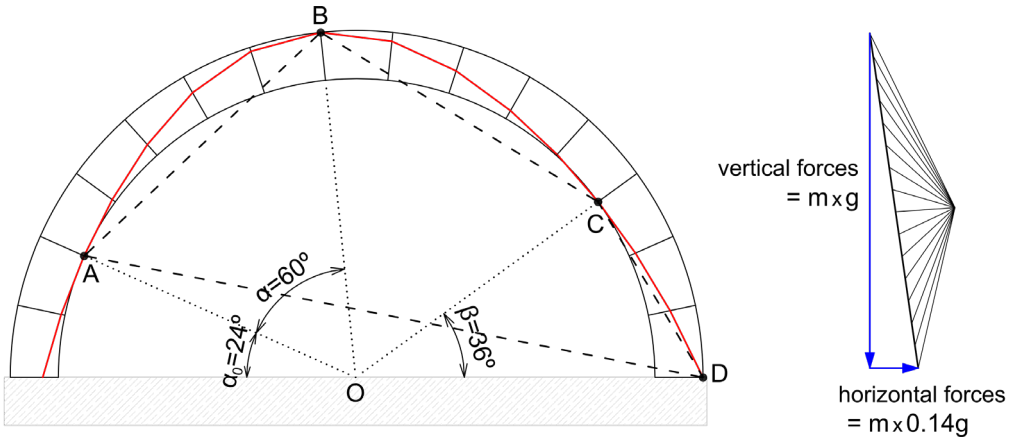

Fig. 8 Minimum-acceleration 4-link collapse mechanism for a discretized zero-tension voussoir arch with $t/r_m = 0.15$ and 15 voussoirs, computed by static-equivalent limit analysis: in red, thrust-line; in blue, acting static-equivalent forces as part of the corresponding polygon of forces.

Shaking table tests have been performed on voussoir arches with similar span and $t/r_m = 0.15$, applying the same form of base motion, by Albuerne et al (2013). Voussoir arches also rocked and collapsed by forming four-link mechanisms, but there are significant differences in behaviour with quasi-brittle arches:

- In quasi-brittle arches two of the fours hinges open at the supports (*A* and *D*) as a result of the finite tensile strength along the arch, while in voussoir arches these hinges are free to form at other points, as observed in shaking table tests.
- When the voussoir arch rocks, the mirror mechanism tends to form when motion reverses, which requires different joints to open when motion reverses (see Fig. 9). On the contrary, in quasi-brittle arches, exactly the same cracks serve as joints when the motion reverses, resulting in two different mechanisms forming, depending the direction of the rocking.
- The travelling hinge phenomenon is observed in voussoir arches, while this is not present in quasi-brittle arches.

Figure 9 also illustrates the difference in location of the 'internal' hinges *B* and *C* between voussoir and quasi-brittle arches.

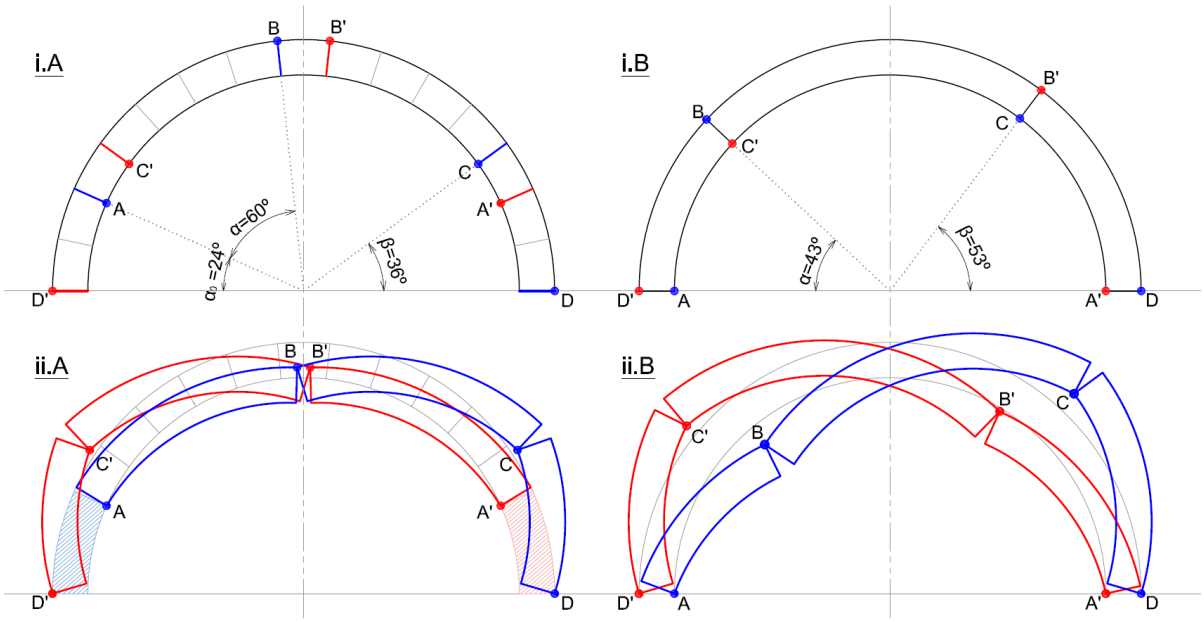

Fig. 9 Comparison of failure mechanism between voussoir (A) and quasi-brittle (B) arches, for t/r_m = 0.15: initial mechanism (in blue) and reverse mechanism (in red). Voussoir arch mechanism based on static-equivalent limit analysis (Fig. 8)

4. Non-linear Finite Element models of undamaged arches

4.1. Description of Finite Element Model

The numerical model is developed with the Finite Element (FE) commercial software Abaqus 2017 (Abaqus 2014). The Abaqus/Explicit dynamic analysis algorithm is used which applies a consistent, large-displacement theory that allows large rotations and large deformations. The explicit algorithm marches a numerical solution forward through time in small time increments without solving a coupled system of equations at each increment nor forming a global stiffness matrix, which often becomes ill-conditioned under extensive material damage. This makes it a stable and computationally efficient algorithm for analysing highly nonlinear and transient dynamic behaviours (Abaqus 2014; Karapitta et al. 2011). The numerical modelling presented in this work follows the continuum mechanics approach, broadly used for quasi-brittle materials such as unreinforced concrete, adobe and masonry (Lourenço et al. 2007; Pelà 2008; Roca et al. 2010; Tarque et al. 2014)

A two-dimensional model of the concrete arch and the steel base is created. Structured mesh with the four-node reduced integration plane stress elements CPS4R is used. The mesh size varies between 9.5 and 11 mm. Using reduced integration elements and having multiple elements across the thickness helps avoiding shear locking and hourglass phenomena which can affect slender structures under bending load (Belytschko et al. 1984; Zienkiewicz et al. 1971). The steel base is modelled with linear elastic properties whereas the Concrete Damage Plasticity (CDP) smeared-crack model is used for the mortar arch. In this material law, the stress-strain curves of the material are treated separately for tension and compression. CDP has been based on the on the work of Lee & Fenves (1998) and Lubliner et al. (1989) and has been widely used in analysis of historic structure made of quasi-brittle materials such as roman concrete (Ivancic, Brune, & Perucchio, 2014) and masonry with a degree of cohesion (Humberto et al., 2013; Milani & Valente, 2015; Silva, Lourenço, & Milani, 2017).

Regarding the properties of the CDP model, the concrete dilation angle (ψ) and K parameter are equal to 30° and 0.666 respectively. The compressive strength of the concrete is taken as 10 MPa. Since in the experimental campaign the concrete arch is observed to break due to tensile stresses, the stress-strain curve for tension is the most influential parameter of the CDP model. Linear tension softening

(see Fig. 10) is adopted for the post-peak stress-strain branch of the tension curve (Abaqus, 2014; Hillerborg et al. 1976). The softening branch of the curve is calculated from the tensile fracture energy (G_f). According to this law, when the maximum principal stress exceeds the tensile strength (f_t), a crack is formed in the plane orthogonal to the direction of principal tensile stress. Various combinations of f_t and G_f, based on the material characterisation of the tested arches, are considered for the numerical analysis (see Fig. 12).

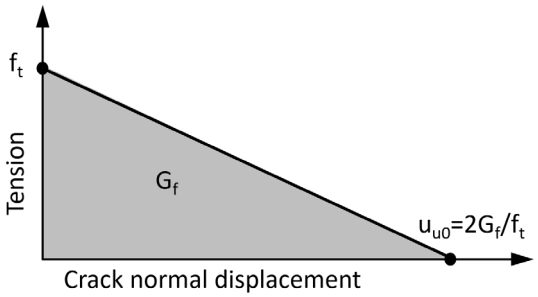

Fig. 10. Linear tension softening; where u_{u0} is the crack normal displacement at which complete loss of tensile strength takes place.

The base motion is applied as horizontal displacements on the steel base of the FE model, whereas the steel base is fixed in the vertical direction. A sufficiently small time-step of 0.0001s is used for the discretisation of the input motion. The contact surfaces between the arch and the steel base are governed by Coulomb friction law with an assumed friction angle equal to 12° (μ = 0.2) and zero cohesion, based on qualitative observations of low friction during experimentation. A lateral gap of around 0.5 mm is introduced between the arch and the intrados and extrados brackets that are modelled as part of the steel base. This gap is modelled to represent the irregularities present at arch supports in the experimental configuration that led to small amounts of relative displacement between the arch specimen and the shaking table. The support configuration in the FE model also allows rocking at the supports similar to the structural behaviour manifested during the shaking table tests.

The model investigates the development of the failure pattern and specifically the formation of the first crack. There are two limitations for using the model for prediction of formation of second crack and, moreover, for prediction of collapse. One limitation is the characterization of crack growth in the experimental material, lime mortar: the material law used has been developed for concrete, which, in spite of similarly being a quasi-brittle material, has a different internal macro and micro structure to that of lime mortar. As such, there may be differences in the rate of growth of a crack between the two materials that could have a significant impact on the formation of subsequent cracks under dynamic loading. The second limitation is the fact that, once a crack is fully developed, the FE code is unable to treat that crack as a new dry-contact surface. This affects the way the crack responds to large displacements, which can be of significance in a shaking table test of the nature of those being modelled. As a result, the details of the formation of the second and any subsequent cracks will not be examined closely.

4.2. Modelling the formation of the first crack

FEM analysis of tested arch model

The non-linear FE model is tested and calibrated against experimental test FL9, the details of which, including arch motion and geometry of failure mechanism, are given in Fig. 6 and Table 2. The input motion applied to the model is that experienced by the arch on the shaking table test, amplified until

failure of the model is observed. The lime mortar batch used for the fabrication of this arch, with lime-sand-water ratio of 1–3.2–0.88, is characterised by a single three-point bending test, yielding a value of tensile strength f_t of 0.516 MPa and fracture energy G_f of 8.645 Nm/m^2. These values fall comfortably within the range of material tests results obtained for the mortar. Because a single sample was tested, the characteristic (mean) values obtained for the material are used in the FE model (f_t = 0.426 MPa; G_f = 7.85 Nm/m^2).

Figure 11 summarises the results obtained from the FE analysis. The overall shape of the failure mechanism matches that observed in the experiment in that hinges *A* and *D* form at the supports, with the first hinge forming by cracking the material.

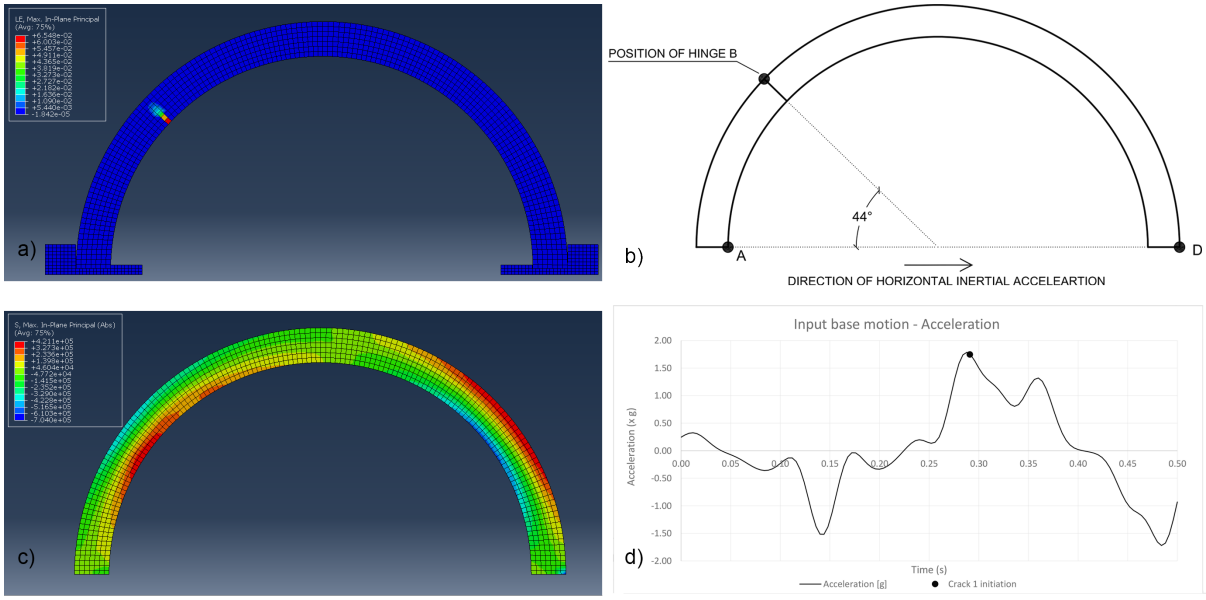

Fig. 11. Non-linear FE results for model of tested arch FL9: a) arch numerical model showing the formation of the first crack; b) position of the formation of the first crack; c) stress distribution at the initiation of first crack; d) input motion, indicating the time of formation of first crack.

The FE model is aimed at predicting the formation of the first crack, where agreement between analysis model and experiment is very close. The first crack forms hinge *B*, with the crack initiating on the intrados at an acceleration peak of the input motion. The model predicts the formation of the crack at an angle of 44º from the closest support (hinge *A*), which compares well with the experimental result of 43º. The model overpredicts the acceleration at which the crack forms by approximately 23%, with the first crack forming at a base acceleration of 1.75g while in the shaking table test the crack opened when the arch experienced an acceleration of 1.42g.

The analysis is repeated for the material parameters obtained for the FL9 batch sample given above, obtaining a very similar result. Cracking acceleration is 1.74g and hinge *B* forms at an angle of 40º from hinge *A*.

There are two factors that can explain the overprediction in acceleration at failure. The first is the existence of imperfections and irregularities in the physical sample subject to experimental testing. The second is the fact that the material properties are characterised by a single material sample, while it has been observed that there is an inherent variability in the properties of the material and this sample could have overestimated the characteristic strength of the mortar batch.

Parametric variations of tensile strength f_t and fracture energy G_f

A parametric study of the behaviour of the circular arch under base motion varying the tensile capacity of the material is carried out in order to explore how the tensile capacity affects the response of a masonry material under dynamic loads. The tensile capacity is defined by two parameters, the tensile strength f_t and the fracture energy G_f, both of which are required for defining the material law used in the model, CDP.

The three-point bending tests carried out to characterise the material evidenced a correlation between tensile strength and fracture energy (Fig. 12). A parametric variation of tensile strength is proposed, adjusting the fracture energy using a linear correlation as shown in Fig. 12. In addition, the effect of the fracture energy in the model is studied by considering two series of variation of fracture energy at constant tensile strength: 1) f_{tl} = 0.516 MPa, the tensile strength for the tested arch FL9; and 2) f_{tk} = 0.426 MPa, the lime mortar characteristic strength. The tested series are also shown in Fig. 12.

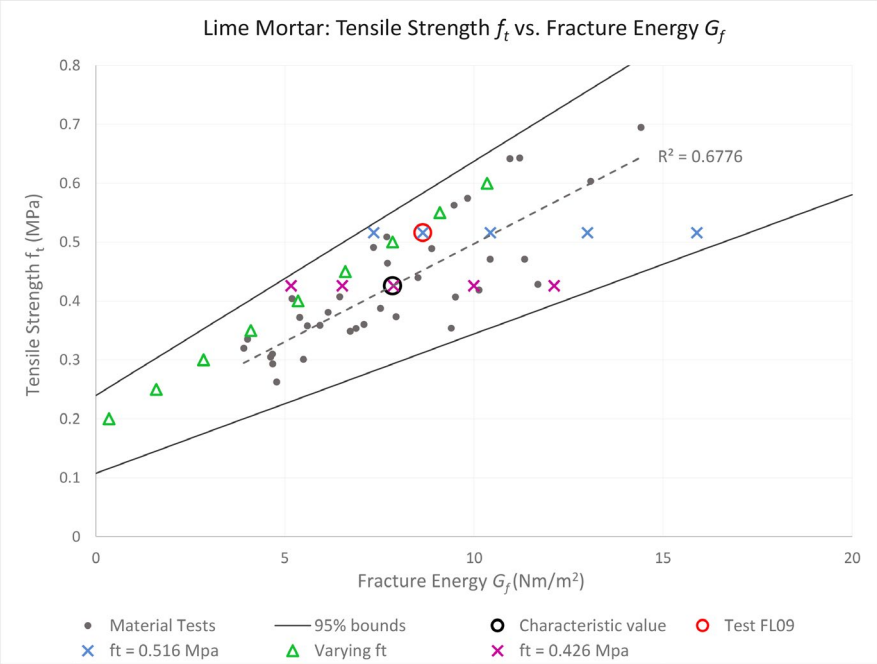

Fig. 12. Lime mortar material tensile strength f_t vs. fracture energy G_f, presenting material characterisation test results (in black) and values adopted for FE analysis (in colour).

The results of the variation of tensile strength with adjusted fracture energy according to a linear relationship are summarised on Fig. 13, where the horizontal acceleration at crack initiation is plotted against the tensile strength. A linear variation can be seen in the lower section of the curve, while a plateau in horizontal acceleration at crack formation is reached as the tensile strength increases.

The dynamic nature of the load results in a constantly changing stress distribution. The peak tensile stress continuously shifts along the arch as the ratio between vertical and horizontal inertial loads changes. In the presence of horizontal acceleration, the stress distribution is asymmetric, with the point of maximum sagging bending shifting from midspan to the windward side of the arch for the given verse of the applied acceleration.

A point of maximum hogging bending appears, displaced from the midspan in the opposite direction. Sagging bending generates tensile stresses on the intrados, i.e. leading to hinging about the extrados. This hinge, which corresponds to hinge *B* (Fig. 11) is the first one to materialise in the analysis, as was seen for FL9, with the first crack initiating on the intrados of the arch, displaced from the midspan of

the arch. This behaviour agrees very well with the observations from experimental tests. In the analyses, all first cracks were contained in a small arch segment ranging from 43º to 58º from hinge *A* (Fig. 13). The position of the crack appears to depend on the tensile capacity of the material. For lower capacities, hinge *B* forms further from the support and closer to the value of the *AOB* angle for zero tensile capacity (Fig. 8). This angle reduces as the tensile capacity increases, stabilising around 45º for the larger capacity values analysed.

In the experimental tests the position of hinge *B* was recorded to fall within an arch segment ranging from 43º to 67º from hinge *A* (Fig. 7). This bigger spread in experimental tests can be explained by the possible existence of material imperfections that can result on weak points where cracks can more readily form.

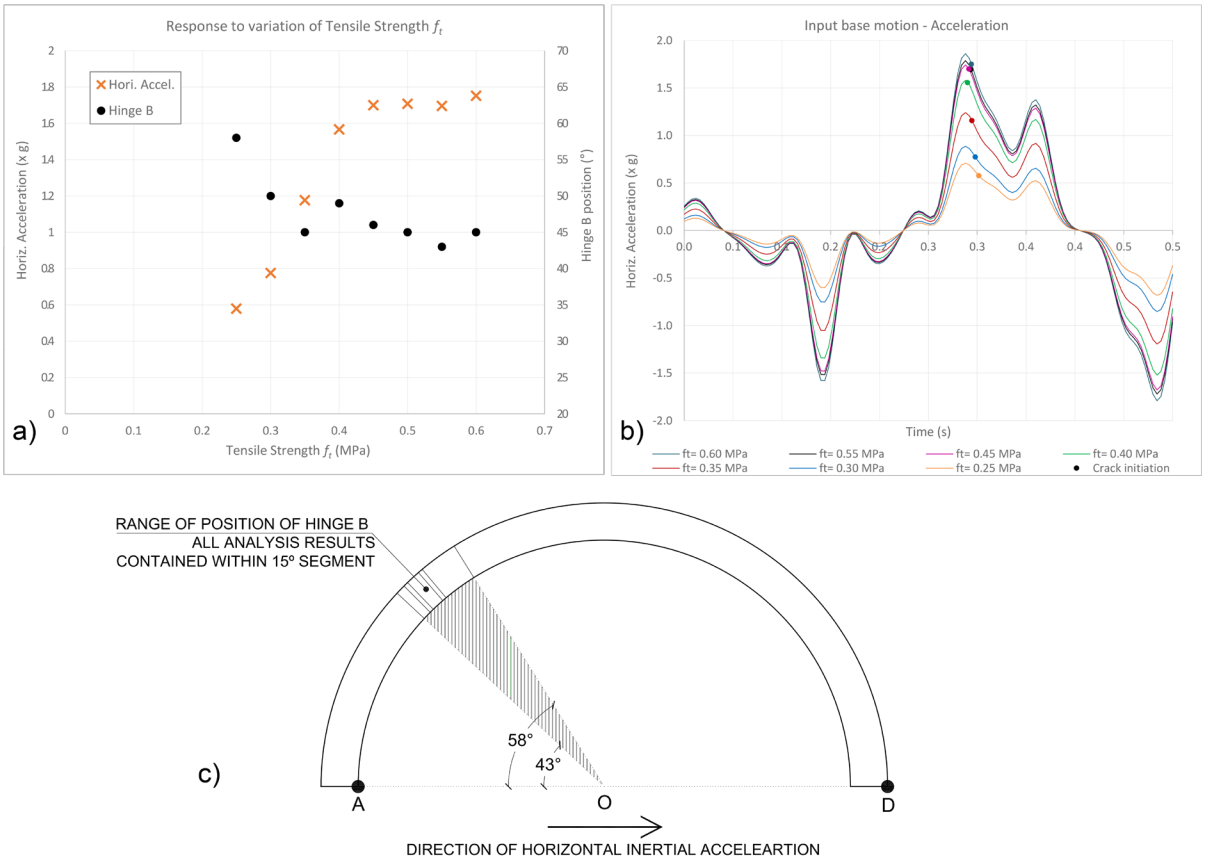

Fig. 13. Summary of non-linear FE models of failure of continuous arches for variation in tensile strength f_t: a) Horizontal acceleration at initiation of first crack vs. tensile strength f_t; b) input motion at failure for selected values of tensile strength f_t, giving the point of initiation of the first crack; c) position of first cracks, corresponding to hinge *B* in all cases.

The results of the parametric variations of fracture energy for constant tensile strength are presented in Fig. 14. The values of fracture energy are evenly spread within the 95% bounds of the material characterisation tests (see Fig. 12). The results evidence a strong dependence of crack formation on fracture energy, highlighting the importance of this parameter in the behaviour of masonry with non-negligible tensile capacity. The position of the crack, however, does not show a strong correlation with fracture energy variation, suggesting that position may be more strongly related to the tensile strength.

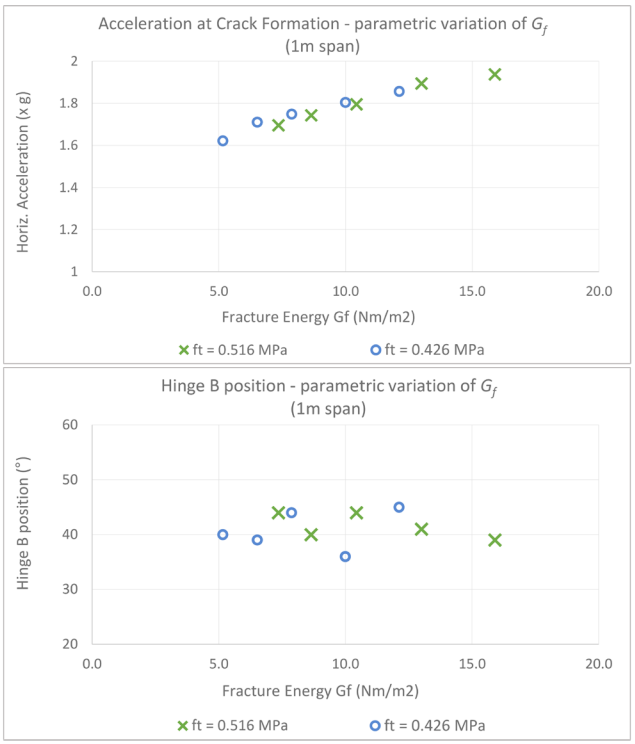

Fig. 14. Summary of non-linear FE models of failure of continuous arches for variation in fracture energy G_f. Top: Horizontal acceleration at initiation of first crack vs. fracture energy G_f; bottom: Hinge *B* position vs. fracture energy G_f.

4.3. Simplified static-equivalent analysis of pre-cracked arches

When the first crack opens in the mortar arch, there is a sudden drop in strength at the cross section of the crack and internal stresses experience an immediate redistribution. Furthermore, the formation of this first crack generates a 3-pinned arch. In this condition the arch can be simplified as a statically determinate 1D structure that can be analysed using equilibrium equations only (Fig. 15).
This simplified model is used for predicting the position of the second and final crack, the crack that becomes the fourth hinge in the arch and turns it into a mechanism.

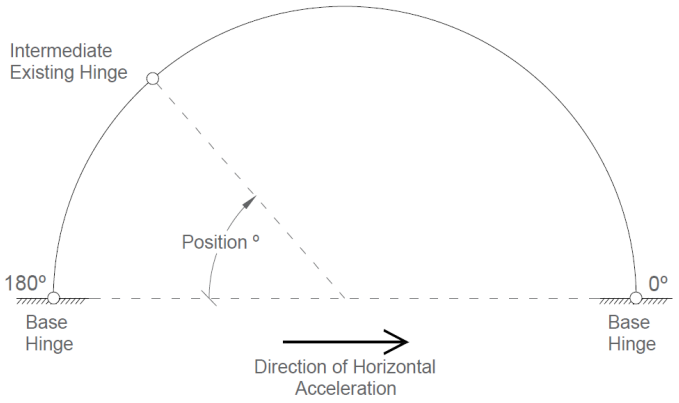

Fig. 15. Simplified structural model of 3-pinned arch for the analysis of the cracked arch to estimate the position of the formation of the second and final crack.

The formation of the final crack has been computed for all arches subject to shaking table tests given in Table 1. The first crack is treated as a hinge and the simplified structural model is subject to the inertial loads resulting from gravity and from the lateral acceleration that has generated the first crack. Under these loads, the point of maximum tensile stress is taken as the estimate of the position where the final crack will form. The predicted position is given in Fig. 16.

These results evidence that the simplified 1D statically-determinate model is appropriate for predicting the formation of the fourth hinge in the structure, with 50% of predictions lying within 5º of the experimental observations and 80% of predictions being within 10º of the experiments.

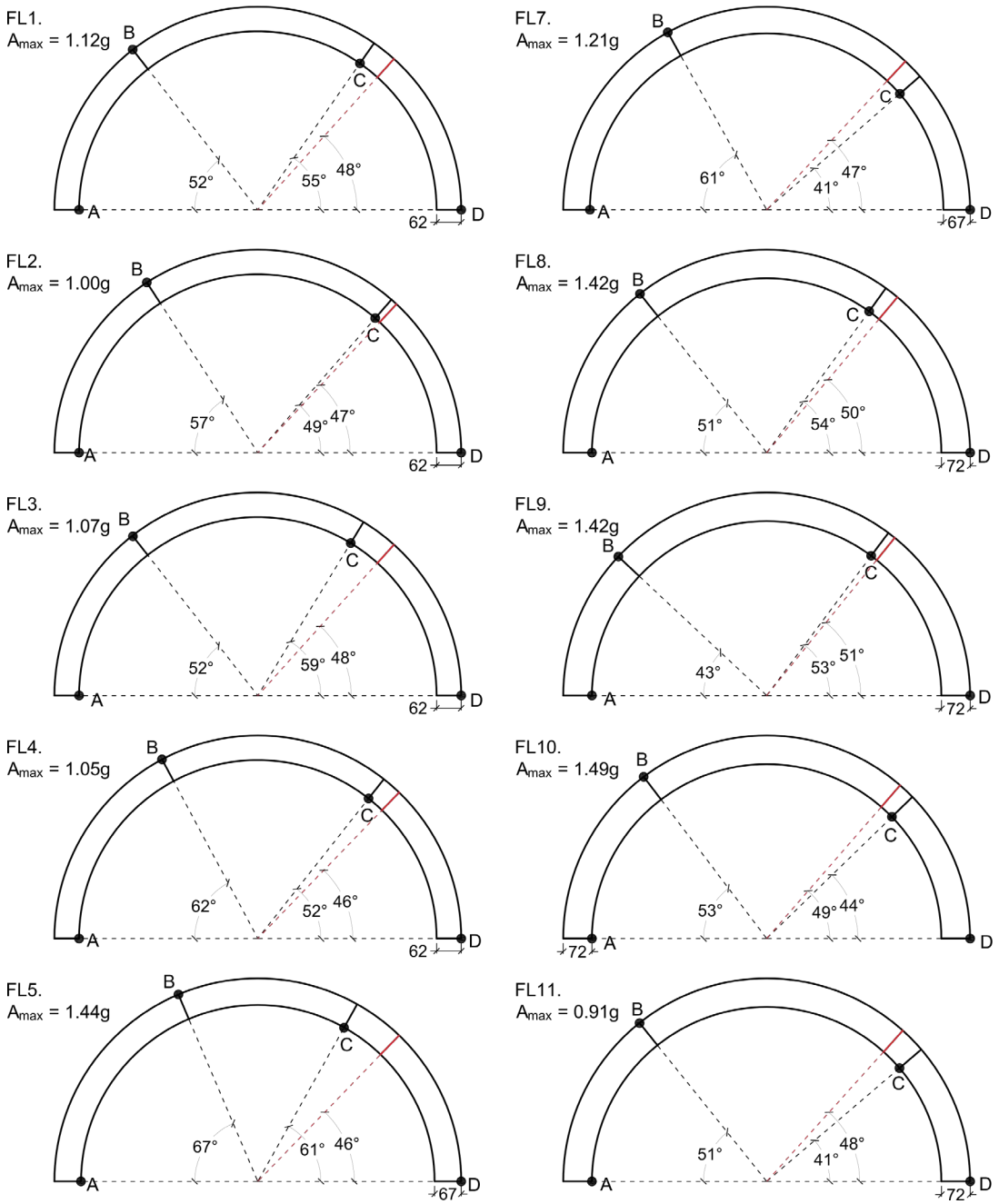

Fig. 16. Predicted position for the formation of second and final crack (in red) for the arches subject to shaking table tests based on the simplified 3-pinned arch model, compared to the observed crack position (in black).

4.4. Modelling the behaviour of full-size arches

It has been shown that the FE model can reliably simulate the results of the experimental tests of specimens, which are scaled representation of prototypes 2-3 times larger (section 3.2). With the intention of better understanding how real masonry structures behave under seismic loading, a second FE model is created to represent full-size structures and to capture more realistic characteristics.

The size of the model is increased to 4m in order to represent 4m span real arches. The tensile strength of the material is increased to f_{t2} = 0.820 MPa, the average value of existing experimental results for Roman concrete in the literature (Table 1), representative of real full-size structures. The fracture energy for this tensile strength is computed to be G_f = 16.25 Nm/m^2, in accordance with the correlation established from the material data in Fig. 12. The contact properties between the arch and the base are also modified to replace the laboratory conditions of an arch resting on a smooth metal plate. The coulomb friction coefficient μ is raised from 0.2 to 0.7, a value that falls in the range of results for experimental characterization of masonry joints (Vasconcelos et al. 2008, Jafari et al. 2017).

Failure occurs at a base horizontal acceleration of 0.73g. The failure pattern observed in the full-size arch model is similar to that of the scale model, with the first crack opening at 58° from hinge *A* at the support (Fig 17, top), which lies within the range of crack formation positions observed experimentally and agrees with the trend observed numerically for the specimen arches, with larger angles for proportionately lower tensile capacities (Fig. 13). A small degree of sliding of the arch with respect to the supporting base occurs as a result of the discontinuity at the support, as observed in the scaled arches. Increasing the coefficient of friction to assimilate masonry joints reduces the sliding velocity of the large arches, thus introducing a difference in dynamic behaviour with respect to the analysis of scaled arches. This results in differences in the instant of crack formation observed in the acceleration signal (Fig. 17, bottom).

Applying the simplified analysis for pre-cracked (3-pinned) arches described above, the second crack and final hinge (hinge *C*) opens at 45º from hinge *D* at the support. This final mechanism differs significantly from the mechanism for the zero-tension similar arch given in Fig. 8.

This model supports the relevance of the experimental observations that the presence of low tensile capacity in masonry arches has a significant impact in the structural response to dynamic horizontal loading, resulting in the formation of a mechanism that is different to that of a zero-tension arch and that requires the formation of hinges through fracture of the material.

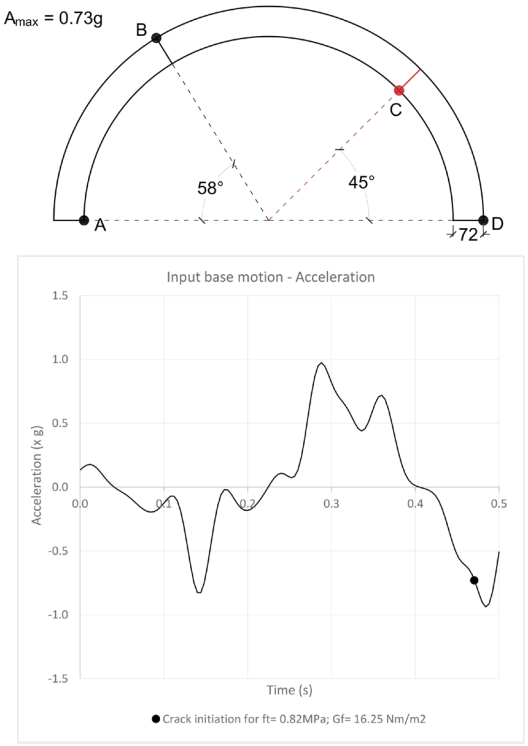

Fig. 17. Summary of results of analysis of 4m span FE model, tensile strength f_{t2} = 0.820 MPa and fracture energy G = 16.25 Nm/m^2. Top: position of first crack corresponding to hinge B as predicted numerically and position of final crack corresponding to hinge C predicted analytically based on 3-pinned arch model; bottom: input motion at failure giving the point of initiation of the first crack.

5. Conclusions

The seismic stability of continuous, quasi-brittle arches with a small but non-negligible tensile strength is a subject of great importance in the preservation of historic structures in earthquake-prone regions. Examples include arches, vaults and domes built in Roman concrete, or built with cohesive mortar, such as timbrel vaulting.

Shaking table tests have been performed on quasi-brittle semicircular arches made of lime mortar (hydraulic lime-to-sand volume ratio of 1:3.2) with 1m span to explore the behaviour of masonry arches with non-negligible tensile strength. The lime mortar, which presents a variability in material strength that is typical of quasi-brittle materials, has been characterised to have a tensile strength f_t = 0.426 MPa (SD: 25.3%) and a fracture energy G_f = 7.85 Nm/m^2 (SD: 34.0%). Based on available material tests of samples taken from real existing structures, these experimental arches are representative of real Roman concrete arches 2-to-3 times larger, that is, with a span between 2m and 3m, according to the scaling relationship that the scaling of the tensile strength must be equal to the scaling of the linear dimensions.

Results show clear and consistent patterns of behaviour of these arches that evidence significant effect of the tensile capacity. Arches fail by forming a collapse mechanism and present a degree of variation of failure acceleration (acceleration at formation of first hinge), with SD up to 17.8%, and hinge position that are nonetheless within the inherent variation of the material.

Compared to the geometrically similar no-tension voussoir arch, the tested arches fail at larger peak horizontal accelerations and, while they fail through the formation of a four-link mechanism like the no-tension arch, the position of the hinges is different. Instead of the strongly non-symmetric

mechanism of the non-tension arch, in the tested arches the extreme hinges *A* and *D* open always at the supports and the intermediate hinges *B* and *C* open at cracks located closer to mirror-symmetry about the middle axis (though not perfectly symmetric). Furthermore, failure occurs by the opening of only four hinges fixed in location (two at the supports and two at internal cracks), without the phenomenon of travelling hinges observed consistently in lateral failure of voussoir arches under dynamic loading.

Non-linear FE analysis is used for modelling the failure of the tested arches and determine the level of horizontal acceleration necessary for causing cracking and to estimate the position of the first crack. Abaqus/Explicit dynamic analysis algorithm, from commercial software Abaqus 2017 is used for this analysis, modelling the arch with the Concrete Damage Plasticity numerical material law. Tested arch FL9 is modelled to calibrate the model, obtaining good correlation of the crack position while the failure acceleration is overestimated by roughly 20%, which is explained as an effect of lack of imperfections in the numerical model. CDP material law requires the input of both the tensile strength f_t and the fracture energy G_f of the material, which present a degree of variability characteristic of quasi-brittle materials. Parametric variations of both properties evidence a strong dependence of the failure acceleration on either parameter. The position of the first crack (hinge *B*), however, is less clearly affected with the first crack opening consistently in the same 15º portion of the arch. A trend between hinge *B* position and material tensile strength is observed, showing hinge *B* to form closer to hinge *A* for higher tensile strengths. The position of the second and final crack is predicted with reasonable agreement by performing a quasi-static analysis of a 3-pin arch simplified model.

A second similar model of a full-size arch with a span of 4m is created to model the behaviour of real arches. The tensile strength is taken as the average of existing experimental tests on real Roman concrete samples and the fracture energy is computed according to the relationship established for the material tests performed on the quasi-brittle lime mortar used in shaking table tests. The failure pattern is similar to that observed in shaking table tests and computed in the scale model, with the first crack opening in the same range of position, at a lower acceleration that is consistent with the increase in size-to-tensile strength ratio.

These novel experiments evidence the effect that low but non-negligible tensile capacity has on the mechanism behaviour of vaulted masonry structures subject to dynamic loading, and the proposed analysis is an initial approximation to modelling this effect. Further experimentation on larger test specimens with proportionately lower tensile capacity would be an insightful next step to continue investigating this behaviour and bound the type of materials and constructions where consideration of tensile capacity in the presence of dynamic loads is necessary.

References

Abaqus (2014) Abaqus documentation - version 6.14, Dassault Systèmes, Providence, RI, USA.

Albuerne, A. (2016) Seismic collapse of vaulted structures: unreinforced quasi-brittle materials and the case study of the Basilica of Maxentius in Rome. *D.Phil. thesis*, University of Oxford.

Albuerne, A., Williams, M.S. (2017) Structural appraisal of a Roman concrete vaulted monument: The Basilica of Maxentius. *Int. J. Archit. Herit*., 11(7): 901-912.

Albuerne, A., Williams, M.S. (2015) Monitoring the seismic performance of arch models using particle image velocimetry. *SECED Conference 2015*, Cambridge.

Albuerne, A., Williams, M.S., Lawson V. (2013) Prediction of the failure mechanism of arches and vaults under base motion using DEM based on the NCSD method. *Wiadomosci Konserw* 34:41-47.

Albuerne, A., Huerta, S. (2010) Coulomb's Theory of arches in Spain ca. 1800: The manuscript of Joaquín Monasterio. ARCH '10, Fuzhou, Oct 2010.

Alexakis, H., Makris, N. (2016) Validation of the Discrete Element Method for the Limit Stability Analysis of Masonry Arches. In Sarhosis, V., Bagi, K., Lemos, J.V., Milani, G. (Eds.) *Computational Modeling of Masonry Structures Using the Discrete Element Method*. Hershey, PA: IGI Global.

Alexakis, H., Makris, N. (2014) Limit equilibrium analysis and the minimum thickness of circular masonry arches to withstand lateral inertial loading. *Arch. Appl. Mech.,* 84:757–772.

Belytschko, T., Ong, J.S.J., Liu, W.K., Kennedy, J.M. (1984) Hourglass control in linear and non-linear problems. *Comput. Methods Appl. Mech. Eng.* 43:251-276.

Boothby, T.E., (2001) Analysis of masonry arches and vaults. *Prog. Struct. Eng. Mater.* 3:246–256.

Brune, P.F. (2010) The Mechanics of Imperial Roman Concrete and the Structural Design of Vaulted Monuments. *Ph.D. thesis*, University of Rochester, NY.

Campillo, M., Gariel, J.C., Aki, K., Sanchez-Sesma, F.J. (1989) Destructive strong ground motion in Mexico City: source, path and site effects during great 1985 Michoacán Earthquake. *Bulletin Seismol. Soc. Amer.,* 79:1718-735.

Casapulla, C., D'Ayala, D. (2001) Lower bound approach to the limit analysis of 3D vaulted block masonry structures. In Hughes, T.G., Pande G.N. (eds.), *Computer Methods in Structural Masonry*; Proc. 5th Intern. Symp., Rome 18-20 April 2001. Swansea (UK): Computers & Geotechnics Limited.

Clemente, P. (1998) Introduction to dynamics of stone arches. *Earthq. Eng. Struct. D.,* 27:513-522.

Couplet, P. (1729) De la poussée des voûtes. Histoire de l'Académie Royale des Sciences, Paris, 79–117 and 117–141

D'Ayala, D., Tomasoni, E. (2008) Three-dimensional analysis of masonry vaults using limit state analysis with finite friction. *Int. J. Archit. Herit*., 5(2):140-171.

De Lorenzis, L., DeJong, M.J., Ochsendorf, J.A. (2007) Failure of masonry arches under impulse base motion. *Earthq. Eng. Struct. D.,* 36**:**2119-2136.

DeJong, M.J. (2009) Seismic assessment strategies for masonry structures. *Ph.D. thesis*, Massachusetts Institute of Technology.

DeJong, M.J., De Lorenzis, L., Adams, S., Ochsendorf, J.A. (2008) Rocking stability of masonry arches in seismic regions. *Earthq. Spectra,* 24**:**847-865.

DeJong, M.J., Ochsendorf, J.A. (2010) Dynamics of in-plane arch rocking: an energy approach. *Proc. Instn Civ. Engrs, Engng & Comp. Mech.,* 163**:**179-186.

Douglas, J., Seyedi, D.M., Ulrich, T., Modaressi, H., Foerster, E., Pitilakis, K., Pitilakis, D., Karatzetzou, A., Gazetas, G., Garini, E., Loli, M. (2015) Evaluation of seismic hazard for the assessment of historical elements at risk: description of input and selection of intensity measures. *Bull. Earthq. Eng.,* 13:49-65.

Gaetani, A., Lourenço, P., Monti, G., Moroni, M. (2017) Shaking table tests and numerical analyses on a scaled dry-joint arch undergoing windowed sine pulses. *Bull. Earthq. Eng.,* 15:4939:4961.

Giavarini, C., Samuelli Ferretti, A., Santarelli, M.L. (2006) Mechanical Characteristics of Roman "Opus Caementicium". In: Kourkoulis, S.K. (Ed.) *Fracture and Failure of Natural Building Stones.*

Athens, Springer.

Giavarini, C., Amici, C.M. (2005) *The Basilica of Maxentius. The Monument, its Materials, Construction, and Stability.* "L'Erma" di Bretschneider, Rome.

Heyman, J. (1969) The safety of masonry arches. *Int. J. Mech. Sci.* 11(4):363-385.

Heyman, J. (1966) The Stone Skeleton. *Int. J. Solids Struct.*, 249-279.

Hillerborg, A., Modéer, M., Petersson, P. E. (1976) Analysis of crack formation and crack growth in concrete by means of fracture mechanics and finite elements. *Cem. Concr. Res.*, *6*(6):773–781.

Huerta, S. (2004) *Arcos, bóvedas y cúpulas. Geometría y equilibrio en el cálculo tradicional de estructuras de fábrica,* Madrid, Instituto Juan de Herrera.

Humberto, V., Tarque, N., Silveira, D., Camata, G., Lobo, B., Blondet, M., … Costa, A. (2013) Structural Behaviour and Retrofitting of Adobe Masonry Buildings. In Costa, A., Guedes, J.M., Varum, H. (Eds.) *Structural Rehabilitation of Old Buildings*, Berlin: Springer-Verlag 37–75.

Ivancic, S., Brune, P., Perucchio, R. (2014) Concrete Damage Plasticity Model For Ancient Roman Pozzolanic Concrete. In *The 9th International Masonry Conference - IMC*.

Jafari, S., Rots, J.G., Esposito, R., Messali, F. (2017) Characterizing the material properties of dutch unreinforced masonry. *Procedia Eng.* 193:250-257.

Karapitta, L., Mouzakis, H., Carydis, P. (2011) Explicit finite-element analyss for the in-plane cyclic behaviour of unreinforced masonry structures. *Earthq. Eng. Struct. D.,* 401:175-193.

Karihaloo, B.L., Huang, X. (1991) Tensile response of quasi-brittle materials. *Pure Appl. Geophys.,* 137**,** 461-487.

Kooharian, A. (1952) Limit analysis of voussoir (segmental) and concrete arches. *J. Am. Concrete Inst.* 49(12):317–328.

Lee, J., Fenves, G.L. (1998) Plastic-damage model for cyclic loading of concrete structures. *J. Eng. Mech.* 124(8):892-900.

Lemos, J.V. (2007) Discrete element modeling of masonry structures. *Int. J. Archit. Herit.* 1(2):190-213.

Lemos, J.V. (2001) Modelling the behaviour of a stone masonry arch structure under cyclic loads. In Hughes, T.G., Pande, G.N. (Eds.) *Computer Methods in Strutural Masonry*. Swansea, UK: Computers & Geotechics Ltd.

Livesley, R.K. (1992) A computational model for the limit analysis of three-dimensional masonry structures. *Meccanica* 27:161-172.

Livesley, R.K. (1978) Limit analysis of structures formed from rigid blocks. *Int. J. Numer. Meth. Eng.,* 12:1853-1871.

Lourenço, P.B., Milani, G., Tralli, A., Zucchini, A. (2007) Analysis of masonry structures: review of and recent trends of homogenisation techniques. *Can. J. Civil Eng.* 34:1443-1457.

Lubliner, J., Oliver, J., Oller, S., Oñate, E. (1988) A plastic-damage model for concrete. *Int. J. Solids Structures* 25(3):299-326.

Makris, N., Alexakis, H. (2013) The effect of stereotomy on the shape of the thrust-line and the minimum thickness of semi-circular masonry arches. *Arch. Appl. Mech.* 83:1511–1533.

Makris, N., Roussos, Y.S. (2000) Rocking response of rigid blocks under near-source ground motions. *Géotechnique*, 50:243-262.

Milani, G., Valente, M. (2015) Failure analysis of seven masonry churches severely damaged during the 2012 Emilia-Romagna (Italy) earthquake: Non-linear dynamic analyses vs conventional static approaches. *Eng. Fail. Anal.*, 54:13–56.

Ochsendorf, J. (2002) *Collapse of masonry structures*. Ph.D. thesis, University of Cambridge.

Oppenheim, I.J. (1992) The masonry arch as a four-link mechanism under base motion. *Earthquake Engng Struct. Dyn.,* 21:1005-1017.

Otto, F. (1983) Der Bogen, Teil 3: Eine Arbeit des Instituts für leichte Flächentragwerke. *Arcus,* 1983**:** 199-207.

Pelà, L. (2008) *Continuum damage model for nonlinear analysis of masonry structures*. Ph.D. thesis, Università degli Studi di Ferrara.

Planas, J., Elices, M. (1985) Fractura del hormigón en regimen no lineal. Intentos para medir la energía de fractura Gf. *Informes de la Construcción,* 37**:**35-52.

Pulatsu, B., Erdogmus, E., Lourenço, P.B., (2019) Simulation of Masonry Arch Bridges Using 3D Discrete Element Modeling. In: Aguilar R., Torrealva D., Moreira S., Pando M.A., Ramos L.F. (eds) *Structural Analysis of Historical Constructions,* RILEM Bookseries, vol 18. Springer, Cham.

Ramaglia, G., Lignola, G.P., Prota, A. (2016) Collapse Analysis of slender masonry barrel vaults. *Eng. Struct.*, 117:86-100.

Roca P., Cervera M., Gariup G., Pelà L. (2010) Structural analysis of masonry historical constructions. Classical and advanced approaches. *Arch. Comput. Methods Eng.*, 17(3):299-325.

Rodriguez del Viso, J. (2008) Comportamiento mecánico en fractura del hormigón de alta resistencia y su variación con la velocidad de solicitación. *Escuela de Ingenieros de Caminos, Canales y Puertos de Ciudad Real.* Ciudad Real, Universidad de Castilla-La Mancha.

Samuelli Ferretti, A. (2000) Opus Caementicium, the Roman concrete. Domus Aurea and Basilica of Maxentius: stress analysis and safety. *12th Int. Conf. on Brick/Block Masonry*, Madrid.

Shah, S.P., Ouyang, C. (1994) Fracture mechanics for failure of concrete. *Annual Review of Material Science,* 24**:**293-320.

Silva, L. C., Lourenço, P. B., Milani, G. (2017) Nonlinear Discrete Homogenized Model for Out-of-Plane Loaded Masonry Walls. *J. Struct. Eng.*, 143(9).

Smars, P. (2008) Influence of friction and tensile resistance on the stability of masonry arches. In D'Ayala, D., Fodde, E. (eds) *Structural Analysis of Historic Construction*. London: Taylor & Francis Group.

Smars, P. (2000) *Etudes sur la stabilité des arcs et voûtes, confrontation des méthodes de l'analyse limite aux voûtes gothiques en Brabant*. Ph.D. thesis, K.U.Leuven.

Tarque, N., Camata, G., Spacone, E., Varum, H., Blondet, M. (2014) Nonlinear dynamic analysis of a full-scale unreinforced adobe model. *Earthquake Spectra* 30(4):1643-1661.

Vasconcelos G., Lourenço P.B., Oliveira D. (2008) Experimental shear behaviour of stone masonry joints. In D'Ayala, D., Fodde, E. (eds) *Structural Analysis of Historic Construction*. London: Taylor & Francis Group.

White D.J., Take W.A., Bolton M.D. (2003) Soil deformation measurement using particle image velocimetry (PIV) and photogrammetry. *Geotechnique,* 53**:**619-631.

Williams M.S., Albuerne A., Lawson V., Yip F. (2012) Model scale shaking table tests on masonry barrel and cross vaults. *15th World Conf. on Earthquake Engng*, Lisbon, Portugal.

Zhang J., Makris N. (2001) Rocking response of free-standing blocks under cycloidal pulses. *J. Eng. Mech.*, 127(5):473-483.

Zienkiewicz O.C., Taylor R.L., Too J.M. (1971) Reduced integration technique in general analysis of plates and shells. *Int. J. Numer. Methods Eng.* 3:275-290.